Journal of Materials Chemistry A

Accepted Manuscript

ROYAL SOCIETY OF CHEMISTRY

www.rsc.org/materialsA

Carbon nanotube decorated with nickel phosphide nanoparticles as efficient nanohybrid electrocatalyst for enhanced hydrogen evolution reaction

Yuan Pan, Wenhui Hu, Dapeng Liu, Yunqi Liu, Chenguang Liu**

State Key Laboratory of Heavy Oil Processing, Key Laboratory of Catalysis, China National Petroleum Corporation (CNPC), China University of Petroleum, 66 West Changjiang Road, Qingdao, Shandong 266580, P. R. China

* Corresponding author. E-mail address: liuyq@upc.edu.cn; cgliu1962@sina.com

Tel.: +86-532-86981861; +86-532-86981716.

Abstract

Designing efficient, stable and inexpensive electrocatalysts to replace Pt-based catalysts for the hydrogen evolution reaction (HER) is highly desired in renewable energy research. In this study, we report the synthesis of nickel phosphide nanoparticles decorated on multiwall carbon nanotubes (Ni_2P/CNT) by in situ thermal decomposition of nickel acetylacetonate as nickel source and trioctylphosphine as phosphorus source in oleylamine solution of CNT. As novel HER electrocatalyst, the Ni_2P/CNT nanohybrid exhibits excellent electrocatalytic activity in 0.5 M H_2SO_4 with low onset overpotential (88 mV), a small Tafel slope (53 $mV \cdot dec^{-1}$), a high exchange current density (0.0537 $mA \cdot cm^{-2}$) and good stability. It only needs overpotentials of 98 and 124 mV to attain current densities of 2 and 10 $mA \cdot cm^{-2}$, respectively. In addition, the Ni_2P/CNT nanohybrid shows nearly 100% Faradaic efficiency in acid solutions. This work successfully demonstrates that the introduction of Ni_2P NPs into CNT for enhanced electrocatalytic properties is feasible, and that this may open up a potential way for designing more efficient Ni_2P-based catalysts for HER.

Keywords: Carbon nanotube; nickel phosphide nanoparticles; electrocatalyst; hydrogen evolution reaction.

Introudction

With the increase of global energy demand and the aggravation of environmental problems, more and more attention is being paid to the production of hydrogen[1]. Hydrogen is a clean and efficient fuel and it has been regarded as the most promising candidate for replacing fossil fuels in the future[2]. Electrolysis of water is the most efficient, sustainable, and important technology to produce hydrogen[3]. To date, Pt-based catalysts exhibit excellent catalytic activity for the hydrogen evolution reaction (HER) with nearly zero overpotential[4]. However, the high price and scarcity of noble metal limits their application[5]. Therefore, it is important to look for low-cost electrocatalysts for large-scale industrial application.

Transition metal phosphides (TMPs), such as CoP[6], MoP[7], Ni_2P[8], $Ni_{12}P_5$[9] and FeP[10], have been used as effective electrocatalysts to replace the Pt-based noble metal catalyst for HER. In order to improve the electrical conductivity of the catalyst and increase the dispersion of the active phase, several kinds of carbon materials have been used as support, including carbon black, carbon cloth (CC), carbon nanotubes (CNT), carbon flakes (CF) and reduced graphene oxide (RGO). For example, Tian et al.[11] reported a high-activity, acid-stable 3D hydrogen-evolving cathode composed of CoP nanowire arrays on CC via low-temperature phosphidation of the Co(OH)F/CC precursor. Liu et al.[12] prepared a nanohybrid electrocatalyst that consisted of CNT decorated with CoP nanocrystals (NCs) by low-temperature phosphidation of a Co_3O_4/CNT precursor. Cui et al.[13] demonstrated the one-step facile preparation of MoP nanosheets supported on CF via a solid-state reaction. Jiang et al.[14] synthesized

phosphorous-rich FeP_2/C nanohybrid via the pyrolysis of ferrocene and red phosphorus in an evacuated and sealed quartz tube at 500 ^oC. In contrast, reports are very rare on the design and electrocatalytic properties of novel electrocatalysts based on carbon materials decorated with nickel phosphide nanoparticles (NPs). CNT has high surface area and high electrical conductivity, and it has been extensively applied to electrode materials for enhanced electrocatalytic performance[15]. Previously we reported the electrocatalytic properties of nickel phosphide NCs with different phase for HER[16], and we found that the Ni_5P_4 NCs with solid structure exhibited higher catalytic activity than $Ni_{12}P_5$ and Ni_2P NCs. Herein, we describe our recent efforts in developing CNT decorated with Ni_2P NPs to enhance the electrocatalytic activity via an in situ thermal decomposition approach using nickel acetylacetonate ($Ni(acac)_2$) as nickel source and trioctylphosphine (TOP) as phosphorus source in oleylamine (OAm) solution of CNT for the first time. In our experiment, CNT was treated using concentrated nitric acid at 120 ^oC for 12 h because many literature reported that the acid-treated CNT was beneficial for enhanced the catalytic activity. As a novel HER electrocatalyst, the Ni_2P/CNT nanohybrid exhibits excellent electrocatalytic activity in 0.5 M H_2SO_4 with low onset overpotential (88 mV), a small Tafel slope (53 $mV \cdot dec^{-1}$), a high exchange current density (0.0537 $mA \cdot cm^{-2}$) and good stability. It only needs overpotentials of 98 and 124 mV to attain current densities of 2 and 10 $mA \cdot cm^{-2}$, respectively. In addition, the Ni_2P/CNT nanohybrid shows nearly 100% Faradaic efficiency in acid solutions.

Results and discussion

The Ni_2P/CNT nanohybrid was synthesized by an one-pot in situ thermal decomposition reaction of $Ni(acac)_2$ and TOP in an OAm solution of the acid-treated CNT (Scheme 1) at 320 °C for 2 h. During this process, the $Ni(acac)_2$ was reduced to nickel clusters on CNT, then the P-C bonds of TOP broke and phosphorus atoms formed. The Ni_2P/CNT nanohybrid was obtained by the reaction of nickel and phosphorus on CNT. The Ni_2P/CNT nanohybrid was collected by centrifugation and subsequently washed with the mixture of hexane and ethanol several times. The final product was obtained by drying in vacuum at 60 °C for 24 h. For comparison, we also synthesized $Ni_{12}P_5$/CNT and Ni/CNT nanohybrids by changing synthetic conditions (see the Supporting Information for experimental section). Fig. 1 shows the X-ray diffraction (XRD) patterns of CNT, Ni/CNT, $Ni_{12}P_5$/CNT and Ni_2P/CNT. CNT (Fig.1a) shows two diffraction peaks at 26.1° and 42.6°, which can be attributed to the (002) and (101) planes of hexagonal graphite[17]. Ni/CNT (Fig. 1b) shows only one diffraction peak at 44.5°, which was indexed to the (111) plane of the face centered cubic (fcc) nickel (PDF#01-087-0712), indicating that the nickel nanoparticles (NPs) are highly dispersed on the CNT. In addition, the diffraction peaks of $Ni_{12}P_5$/CNT (Fig. 1c) at 32.6°, 35.8°, 38.4°, 40.7°, 41.6°, 44.6°, 47.1°, 49°, 54.2°, 56.1°, 68.6°, 74.5°, 79.8° and 88.9° are attributed to the (310), (301), (112), (202), (400), (330), (240), (312), (510), (501), (161), (004), (262) and (552) planes of the tetragonal structure of $Ni_{12}P_5$ (PDF # 03-065-1623). The diffraction peaks of Ni_2P/CNT (Fig. 1d) at 40.7°, 44.6°, 47.4°, 54.3°, 66.6°, 72.7°, 75.1°, 80.3° and 88.9° are attributed to the (111),

(201), (210), (300), (310), (311), (400), (401) and (321) planes of the hexagonal structure of Ni_2P (PDF # 03-065-3544). Moreover, the great suppression of the (002) plane of CNT was attributed to the loading of Ni, $Ni_{12}P_5$ and Ni_2P NPs with high density[12]. These observations indicate that the CNT was successful decorated with Ni, $Ni_{12}P_5$ and Ni_2P NPs.

The transmission electron microscopy (TEM) image of Ni/CNT (Fig. 2a) nanohybrid reveals that the nickel NPs exhibit monodisperse sphere-like morphology with an average particle size of 6.1±1.3 nm (Fig. S1a). The high-resolution TEM (HRTEM) image (Fig. 2b) reveals that the fringe spacings are about 2.05 Å and 1.77 Å, corresponding to the (111) and (200) lattice planes of fcc nickel. The TEM image of $Ni_{12}P_5$/CNT (Fig. 2c) nanohybrid reveals that the $Ni_{12}P_5$ NPs exhibit hollow structure with an average particle size of 19.4±2.4 nm (Fig. S1b), and the HRTEM image (Fig. 2d) reveals that the fringe spacing is about 1.93 Å, corresponding to the (240) lattice plane of tetragonal $Ni_{12}P_5$. However, the highest intensity (312) lattice plane was not observed from HRTEM, which indicates that the (312) lattice plane was covered by the others planes. The hollow $Ni_{12}P_5$ NPs form in solution from the reaction of Ni NPs with phosphorus, which is liberated from the decomposition of TOP, the obtained phosphorus atoms can diffuse into the nickel NPs via a nanoscale Kirkendall pathway. The outward diffusion rate of nickel is faster than the inward diffusion rate of phosphorus, which leads to the formation of hollow $Ni_{12}P_5$ NPs[16]. The TEM image of Ni_2P/CNT (Fig. 2e) nanohybrid reveals that the Ni_2P NPs exhibit sphere-like morphology with an average particle size of 6.1±1.3 nm (Fig. S1c), and

the HRTEM image (Fig. 2f) reveals that the fringe spacing is about 2.21 Å, corresponding to the (111) lattice plane of hexagonal Ni_2P. Furthermore, one can observe that the Ni, $Ni_{12}P_5$ and Ni_2P NPs are highly dispersed on the outer surface of CNT, as well as uniformly grown inside the CNT. The energy dispersive X-ray (EDX) spectra of the $Ni_{12}P_5$/CNT and Ni_2P/CNT nanohybrids indicate that the measured atomic Ni:P ratios are 2.33:1 (Fig. S2a) and 1.7:1 (Fig. S2b), respectively, which are very close to the stoichiometric ratios of 2.4:1 and 2:1 in $Ni_{12}P_5$ and Ni_2P. Fig. S3 shows the scanning TEM (STEM) image and the corresponding EDX mapping image of C, P and Ni. The results further confirms the good distribution of Ni_2P NPs on the CNT. All these results strongly support the formation of Ni/CNT, $Ni_{12}P_5$/CNT and Ni_2P/CNT nanohybrids by the in situ thermal decomposition approach.

N_2 adsorption-desorption (Fig. S4a) was carried out to further study the surface physical structures. The isotherm belongs to type IV, which is typical for mesoporous material. The Brunauer-Emmett-Teller (BET) specific surface area (SSA) of the as-synthesized Ni_2P/CNT is 59.4 $m^2 \cdot g^{-1}$. However, the BET SSA of the $Ni_{12}P_5$/CNT nanohybrid is 51 $m^2 \cdot g^{-1}$ (Fig. S4c), this value is smaller than that of Ni_2P/CNT, which indicates that the Ni_2P/CNT nanohybrid exposed more active sites. The Barrett-Joyner-Halenda (BJH) pore-size distribution of the Ni_2P/CNT (Fig. S4b) and $Ni_{12}P_5$/CNT (Fig. S4d) show the narrow peak at 3 nm and 3.5 nm, and the average pore-size are 8.55 nm and 12.2 nm, respectively, confirming the nanoporous nature of the Ni_2P/CNT and $Ni_{12}P_5$/CNT nanohybrids.

The chemical states of Ni, P and C in the as-synthesized Ni_2P/CNT were

investigated by X-ray photoelectron spectroscopy (XPS), as shown in Fig. 3. The XPS survey spectrum (Fig. 3a) confirms the elemental composition of Ni_2P/CNT with the peaks of Ni, P, C and O present. For the C 1s energy level, four peaks can be observed at 284.6, 285.4, 286.7 and 289.3 eV (Fig. 3b), which can be assigned to an sp^2 hybridized graphite-like carbon atom, sp^3 hybridized carbon atom, carbon atoms bound to one oxygen atom by a single bond and a double bond, respectively[18]. For the Ni $2p_{3/2}$ energy level, three peaks can be observed at 853.5, 856.3 and 860.9 eV (Fig. 3c), which can be attributed to Ni in Ni_2P, oxidized Ni species and the satellite of the Ni $2p_{3/2}$ peak[19]. For the Ni $2p_{1/2}$ energy level, three peaks are observed at 870.6, 874.5 and 880.2 eV (Fig. 3c), corresponding to Ni in Ni_2P, oxidized Ni species and the satellite of the Ni $2p_{1/2}$ peak, respectively. For the P 2p energy level, two peaks at 129.8 and 133.8 eV can be observed (Fig. 3d), which can be assigned to P in Ni_2P and oxidized P species formed on the surface of Ni_2P/CNT nanohybrid due to air contact[20]. The Ni $2p_{3/2}$ peak at 853.5 eV is very close to that of Ni metal, which indicates that the Ni species in Ni_2P has a very small positive charge ($Ni^{\delta+}$, $0<\delta<2$). The P 2p binding energy at 129.8 eV is less than that of elemental P (130.2 eV), which indicates that the P species in Ni_2P has a very small negative charge ($P^{\delta-}$, $0<\delta<1$). Thus it can be concluded that there is an electron transfer from Ni to P[21], and a small charge indicates a mainly covalent character with small ionic contribution. Furthermore, the $Ni_{12}P_5$/CNT has similar C 1s, Ni 2p and P 2p energy levels as Ni_2P/CNT (Fig. S5), but the positive charge of Ni in $Ni_{12}P_5$/CNT is lower than that of Ni_2P/CNT[16].

The HER catalytic activity of Ni_2P/CNT nanohybrid was evaluated by the

electrochemical experiment in 0.5 M H_2SO_4 with a slow scan rate of 5 $mV \cdot s^{-1}$ using a three-electrode setup with the working electrode prepared by the deposition of the nanohybrid on glassy carbon electrode (GCE). Fig. 4a shows the linear sweep voltammetry (LSV) curve of Ni_2P/CNT in 0.5 M H_2SO_4 with a scan rate of 5 $mV \cdot s^{-1}$. Bare GCE, CNT, $Ni_{12}P_5$/CNT, Ni/CNT and commercial Pt/C were also studied for comparison. It can be seen that the bare GCE and CNT exhibit very small HER activity. Typically, the Pt/C catalyst exhibits the highest HER catalytic activity with nearly zero overpotential. It is surprising that the Ni_2P/CNT exhibits high catalytic activity with low onset overpotential of 88 mV for HER. When the HER current density reached 2 and 10 $mA \cdot cm^{-2}$, the overpotentials were 98 and 124 mV, respectively. We also synthesized $Ni_{12}P_5$/CNT and Ni/CNT nanohybrids as reference electrocatalysts. $Ni_{12}P_5$/CNT shows lower HER activity than that of Ni_2P/CNT, with onset overpotential of 121 mV, but higher than that of Ni/CNT with onset overpotential of 157 mV. Generally, the loading of activity phase on the catalyst is very important in activity comparison. Therefore, the element contents of Ni and P in $Ni_{12}P_5$/CNT and Ni_2P/CNT nanohybrids were estimated by inductively coupled plasma-mass spectrometry (ICP-MS) analysis (Table 1). It can be seen that the element contents of Ni and P in Ni_2P/CNT nanohybrid are less than that of $Ni_{12}P_5$/CNT nanohybrid, but the former exhibits higher catalytic activity. In other words, the percentage of CNT in Ni_2P/CNT nanohybrid is higher than that of $Ni_{12}P_5$/CNT nanohybrid. The improvement of catalytic performance probably due to the high CNT content in Ni_2P/CNT nanohybrid. Table S1 compares the HER

performance of the Ni_2P/CNT nanohybrid with some reported non-noble-metal catalysts, such as CoP/CNT[12], MoS_2/RGO[22], Mo_2C/CNT[23], MoP-CA2[24], MoS_2/FTO[25], MoS_3/FTO[26], $CoSe_2$ NP/CP[27], MoN/C[28], NiMoNx/C[28], WS_2/rGO[29], CoP/Ti[30], CoP/CC[11], Ni_2P/Ti[31], NiP_2 NS/CC[32], $MoSe_2$/RGO[33], Mo_2C/XC[23], MoP/CF[34], Cu_3P NW/CF[35], FeP NA/Ti[36], FeP NAs/CC[37]. From Table S1, one can observe that the overpotentials of the Ni_2P/CNT nanohybrid compare favorably to the behavior of other non-noble-metal catalysts.

Tafel plots can be used to explain the reaction mechanism of HER. The Tafel plots (Fig. 4b) were recorded with the linear regions fitted to the Tafel equation (η = a + b log j, where b is the Tafel slope and j is the current density). This yielded Tafel slopes of approximately 30, 53, 81 and 124 mV·dec^{-1} for Pt/C, Ni_2P/CNT, $Ni_{12}P_5$/CNT and Ni/CNT respectively, which indicates that the HER rate of the Ni_2P/CNT nanohybrid is faster than the rates of the $Ni_{12}P_5$/CNT and Ni/CNT nanohybrids with the increase of potential, and the Pt/C catalyst exhibits the fastest HER rate. According to the mechanism for HER, hydrogen evolution in acidic aqueous proceeds in three steps[38a]. The first step is discharge reaction called Volmer reaction with a Tafel slope of 120 mV·dec^{-1} [Equation (1)], the second step is the ion and atom reaction called Heyrovsky reaction with a slope of 40 mV·dec^{-1} [Equation (2)], the third step is the atom combination reaction called Tafel reaction with a slope of 30 mV·dec^{-1} [Equation (3)]. In our studies, the observed Tafel slopes of Ni_2P/CNT and $Ni_{12}P_5$/CNT were 53 and 81 mV·dec^{-1}, respectively, which indicates that the HER reaction took place via a fast Volmer step followed by a rate-determining Heyrovsky step[38].

$$H_3O^+ + e^- + \text{catalyst} \rightarrow \text{catalyst-H} + H_2O \quad (1)$$

$$H_3O^+ + e^- + \text{catalyst-H} \rightarrow \text{catalyst} + H_2 + H_2O \quad (2)$$

$$\text{catalyst-H} + \text{catalyst-H} \rightarrow 2\text{catalyst} + H_2 \quad (3)$$

Table S2 shows the exchange current density values of the Pt/C, Ni_2P/CNT, $Ni_{12}P_5$/CNT and Ni/CNT nanohybrids, which were calculated by applying the extrapolation method to the Tafel plots (Fig. S6). Ni_2P/CNT displayed an exchange current density of 0.0537 $mA \cdot cm^{-2}$, which further indicates that the catalytic activity of the Ni_2P/CNT nanohybrid is better than that of the $Ni_{12}P_5$/CNT and Ni/CNT nanohybrids.

In order to investigate the intrinsic catalytic activity of the Ni_2P/CNT, $Ni_{12}P_5$/CNT and Ni/CNT nanohybrids, the turnover frequency (TOF) for each active site was then calculated using the reported methods[26]. The number of active sites was determined by CVs (Fig. S7) at a scan rate of 20 $mV \cdot s^{-1}$ over a range of -0.2 to 0.6 V vs. RHE in 1.0 M phosphate buffer solution (PBS, pH = 7). No apparent redox peak was observed, which indicates that this process only one electron transfer occurs, and the integrated charge over the entire potential range should be proportional to the total number of active sites. The calculated active sites number of Ni_2P/CNT, $Ni_{12}P_5$/CNT and Ni/CNT nanohybrids are 2.42×10^{-7}, 8.72×10^{-8} and 5.52×10^{-8} mol, respectively. These values suggest that the Ni_2P/CNT nanohybrid has higher catalytic active sites. Additionally, we quantified the active sites by electrochemistry method[26]. Fig. 4c shows the polarization curves (measured in 0.5 M H_2SO_4) normalized by the active

sites, which are expressed in terms of TOF. To achieve a TOF value of 0.1 s^{-1}, the $Ni_{12}P_5$/CNT and Ni/CNT nanohybrids need an overpotential of about 254 and 336 mV, respectively. However, the Ni_2P/CNT nanohybrid only need an overpotential of about 170 mV, much smaller than that required by the $Ni_{12}P_5$/CNT and Ni/CNT nanohybrids, which further indicates that the Ni_2P/CNT nanohybrid exhibits higher catalytic activity.

We further studied the stability of the Ni_2P/CNT nanohybrid using cyclic voltammetrys (CVs) measurements for scanning 500 cycles with a scan rate of 100 $mV \cdot s^{-1}$ in 0.5 M H_2SO_4, the result inserted in Fig. 4d. The Ni_2P/CNT nanohybrid exhibited good stability in acidic solution with a slight activity loss after 500 cycles. We also found that the current density loss of Ni_2P/CNT was smaller than that of $Ni_{12}P_5$/CNT and Ni/CNT (Fig. S8), which further reveals the excellent catalytic performance of the Ni_2P/CNT nanohybrid. Furthermore, the time-dependent current density curve of the Ni_2P/CNT nanohybrid under static overpotential of 150 mV (Fig. 4d) suggests that the current density has a slight degradation after a long period of 40 000 s. This phenomenon can be explained as follows: 1) the consumption of H^+ led to the decrease of the current density. 2) the HER was inhibited by the remaining hydrogen bubbles on the electrode surface. In addition, the typical serrate shape of the as-measured time-dependent curve was observed, which can be attributed to the accumulation and release of hydrogen bubbles[39].

Electrochemical impedance spectroscopy (EIS) experiments were carried out to investigate the kinetics process of the Ni_2P/CNT nanohybrid in HER. Fig. 5a shows

the Nyquist plots of the Ni_2P/CNT nanohybrid at various potentials. The diameters of the semicircles exhibit the potential-dependent behavior. With the increasing of potentials, the diameter of semicircles decreased gradually, which indicates that the HER kinetics process become faster at higher potential. Fig. 5b shows the Bode plots of the Ni_2P/CNT nanohybrid. These spectra exhibit two-time-constant behavior, and the model equivalent circuit (Fig. S9) was used to fit the experimental data, as shown in Table S3. The value of the solution resistance (R_s) was about 9 Ω, which is nearly potential-independent. However, the value of charge transfer resistance (R_{ct}) is potential-dependent, and the lower R_{ct} reflects the superior electrocatalytic activity of the Ni_2P/CNT nanohybrid. The R_{ct} values also can be used to fit the Tafel slope. In the case where the electron transport resistance at the catalyst/substrate interface or between catalysts is comparable to R_{ct}, the Tafel slope derived from the polarization curve might contain the contribution of electron transport resistance[40]. The Tafel slope of was obtained by fitting the $\log(1/R_{ct})$-η plot of the Ni_2P/CNT nanohybrid, as shown in Fig. 5c. This yielded Tafel slope of about 53 $mV \cdot dec^{-1}$, and this value is in accord with the previous Tafel slope obtained from the polarization curve.

Furthermore, we determined the Faradaic efficiency (FE) of the as-synthesized Ni_2P/CNT and $Ni_{12}P_5$/CNT nanohybrids for hydrogen evolution according to previously reported method[34]. The gas generation was measured quantitatively using a calibrated pressure sensor to monitor the pressure change in the cathode compartment of a H-type electrolytic cell. Galvanostatic electrolysis was carried out with a current density of 20mA cm^{-2} in 0.5 M H_2SO_4 solution. The FE was calculated by comparing

the amount of measured hydrogen with calculated hydrogen (assuming 100% FE), as shown in Fig. 6. The agreement of the amount of experimentally quantified hydrogen with theoretically calculated hydrogen suggests Ni_2P/CNT nanohybrid shows a FE close to 100% for hydrogen evolution. However, the $Ni_{12}P_5$/CNT nanohybrid only exhibits a FE of 83 % after 30 min, which further indicates that the Ni_2P/CNT nanohybrid exhibits higher catalytic activity.

According to the above results, the excellent catalytic activity and stability can be attributed to the following factors: 1) the electronic effect of nickel and the ensemble effect of P. Previously we reported that the positive charge of Ni and the ensemble effect of P in pure Ni_2P nanocrystals are stronger than that of pure $Ni_{12}P_5$ nanocrystals[16], and this reason also can be used to explain the present experiment result. Likewise, Ni/CNT exhibits lower activity than $Ni_{12}P_5$/CNT and Ni_2P/CNT may be due to the low electron valence state of nickel. All results also demonstrate that the HER activity can be improved by introducing phosphorus atom into nickel. 2) when the nickel phosphide NPs supported on CNT, the electrical conductivity of catalyst can be improved, the EIS data (Fig. 5d) shows that the Ni_2P/CNT exhibits a smaller semicircle radius in the Nyquist plot than $Ni_{12}P_5$/CNT and Ni/CNT, which indicates that Ni_2P/CNT has the lowest charge transfer impedance. 3) the Ni_2P NPs supported on the CNT have a small size and thus good dispersity, which means that more active sites are exposed. The catalytic mechanism of transition metal phosphides such as CoP[41], MoP[34], Cu_3P[35] and FeP[36] for HER have been reported. Hydrogenase uses pendant bases proximate to the metal centers as active sites for hydrogen evolution[42].

A metal complex HER catalyst also incorporates proton relays from pendant acid-base groups positioned close to the metal center where hydrogen evolution occurs[43]. Because Ni_2P also has pendant base P in close proximity to the metal center Ni, the nickel centers (δ^+) and the basic phosphorous (δ^-) act as the hydride-acceptor and proton-acceptor centers to promote the HER[44]. Moreover, the phosphorous centers also could promote the formation of nickel-hydride for subsequent hydrogen evolution via electrochemical desorption[45]. Therefore, it is reasonable to conclude that Ni_2P adopts a similar catalytic mechanism with hydrogenase and metal complex catalyst for the HER. In addition, the Ni_2P/CNT exhibits superior HER activity than $Ni_{12}P_5$/CNT also may be due to the Ni_2P/CNT are expected to offer more proton-acceptor centers[32].

Conclusions

In summary, carbon nanotubes decorated with nickel phosphide NPs have been successfully synthesized by in situ thermal decomposition using $Ni(acac)_2$ as the nickel source and TOP as the phosphorus source in OAm solution of CNT. The Ni_2P/CNT nanohybrid exhibits excellent electrocatalytic activity with low onset overpotential (88 mV), a small Tafel slope (53 $mV \cdot dec^{-1}$), a high exchange current density (0.0537 $mA \cdot cm^{-2}$) and good stability. Furthermore, it only needs overpotentials of 98 and 124 mV to attain current densities of 2 and 10 $mA \cdot cm^{-2}$, respectively. Furthermore, the Ni_2P/CNT nanohybrid shows nearly 100% Faradaic efficiency in acid solutions. This study shows that the synthesis of Ni_2P supported on inexpensive and conductive CNT is feasible and has a great potential for the HER.

Similarly, this simple and efficient route also can be applied as a general method to design other electrocatalysts based on carbon materials decorated with transition-metal phosphides.

Acknowledgements

This work was financially supported by the National Natural Science Foundation of China (Grants No. 21006128, 21176258, U1162203), China University of Petroleum for Postgraduate Technology Innovation Project (Grants No. YCX2014033), the Fundamental Research Funds for the Central Universities (Grants No. 15CX06039A) and the Specialized Research Fund for the Doctoral Program of Higher Education of China (Grant No. 20110133110002). We thank Professor R. Prins for helpful comments during the preparation of the manuscript. We also thank postgraduate Wei Cui for his assistance with gas generation experiments.

References

1 B. Hinnemann, P. G. Moses, J. Bonde, K. P. Jørgensen, J. H. Nielsen, S. Horch, I. Chorkendorff, J. K. Nørskov, *J. Am. Chem. Soc.*, 2005, **127**, 5308.

2 (a) M. S. Dresselhaus, I. L. Thomas, *Nature*, 2001, **414**, 332; (b) J. A. Turner, *Science*, 2004, **305**, 972; (c) H. B. Gray, *Nat. Chem.*, 2009, **1**, 7.

3 (a) M. T. M. Koper, *Nat. Chem.*, 2013, **5**, 255; (b) P. D. Tran, M. Nguyen, S. S. Pramana, A. Bhattacharjee, S. Y. Chiam, J. Fize, V. Artero, L. H. Wong, J. Loo, J. Barber, *Energ. & Environ. Sci.,* 2012, **5**, 8912; (c) D. Merki, H. Vrubel, L. Rovelli, S.

Fierro, X. L. Hu, *Chem. Sci.*, 2012, **3**, 2515.

4 (a) M. G. Walter, E. L. Warren, J. R. McKone, S. W. Boettcher, Q. Mi, E. A. Santori, N. S. Lewis, *Chem. Rev.*, 2010, **110**, 6446; (b) D. Merki, X. L. Hu, *Energ. & Environ. Sci.*, 2011, **4**, 3878.

5 (a) M. Arenz, V. Stamenkovic, T. J. Schmidt, K. Wandelt, P. N. Ross, N. M. Markovic, *Surf. Sci.*, 2002, **506**, 287; (b) B. Z. Fang, J. H. Kim, J. S. Yu, *Electrochem. Commun.*, 2008, **10**, 659.

6 E. J. Popczun, C. G. Read, C. W. Roske, N. S. Lewis, R. E. Schaak, *Angew. Chem., Int. Ed.*, 2014, **53**, 5427.

7 P. Xiao, M. A. Sk, L. Thia, X. Ge, R. J. Lim, J. Y. Wang, K. H. Lim, X. Wang, *Energ. & Environ. Sci.*, 2014, **7**, 2624.

8 (a) E. J. Popczun, J. R. McKone, C. G. Read, A. J. Biacchi, A. M. Wiltrout, N. S. Lewis, R. E. Schaak, *J. Am. Chem. Soc.*, 2013, **135**, 9267; (b) L.Q. Feng, H. Vrubel, M. Bensimon, X. L. Hu, *Phys. Chem. Chem. Phys.*, 2014, **16**, 5917.

9 Z. P. Huang, Z. B. Chen, Z. Z. Chen, C. C. Lv, H. Meng, C. Zhang, *ACS Nano*, 2014, **8**, 8121.

10 Y. Xu, R. Wu, J. F. Zhang, Y. M. Shi, B. Zhang, *Chem. Commun.*, 2013, **49**, 6656.

11 J. Q. Tian, Q. Liu, A. M. Asiri, X. P Sun, *J. Am. Chem. Soc.*, 2014, **136**, 7587.

12 Q. Liu, J. Q. Tian, W. Cui, P. Jiang, Ni.Y. Cheng, A. M. Asiri, X. P. Sun, *Angew.*

Chem. Int. Ed., 2014, **53**, 6710.

13 W. Cui, Q. Liua, Z. C. Xing, A. M. Asiri, K. A. Alamry, X. P. Sun, *Appl. Catal. B*, 2015, **164**, 144.

14 J. Jiang, C. Wang, J. Zhang, W. Wang, X. Zhou, B. Pan, K. Tang, J. Zuo, Q. Yang, *J. Mater. Chem. A,* 2015, **3**, 499-503.

15 (a) T. X. Li , J. H. Lee, R. Z. Wang, Y. T. Kang, *Energy*, 2013, **55**, 752. (b) J. Y. Jhan, Y. W. Huang, C. H. Hsu, H. Teng, D. Kuo, P. L. Kuo, *Energy*, 2013, **53**, 282.

16 Y. Pan, Y. Liu, J. Zhao, K. Yang, J. Liang, D. Liu, W. Hu, D. Liu, Y. Liu, C. Liu, *J. Mater. Chem. A,* 2015, **3**, 1656-1665.

17 (a) Q. G. Zhu, A. N. A. Sujari, S. A. Ghani, *J. Electrochem. Soc.*, 2013, **160**, 23; (b) Z. Z. Lu, H. K.Wang, *CrystEngComm*, 2014, **16**, 550.

18 (a) W. Qiu, J. Xia, S. He, H. Xu, H. Zhong, L. Chen, *Electrochim. Acta*, 2014, **117**, 145. (b) Y. Yan, X. Ge, Z. Liu, J. Y. Wang, J. M. Leea, X. Wang, *Nanoscale*, 2013, **5**, 7768.

19 A. P. Grosvenor, S. D. Wik, R. G. Cavell and A. Mar, *Inorg. Chem.*, 2005, **44**, 8988.

20 (a) T. Kor´anyi, *Appl. Catal. A*, 2003, **239**, 253; (b) J. L. Wang, Q. Yang, Z. D. Zhang, S. H. Sun, *Chem. Eur. J.*, 2010, **16**, 7916.

21 P. E. R. Blanchard, A. P. Grosvenor, R. G. Cavell, A. Mar, *Chem. Mater.*, 2008, **20**,

7081.

22 Y. G. Li, H. L. Wang, L. M. Xie, Y. Y. Liang, G. S. Hong, H. J. Dai, *J. Am. Chem. Soc.*, 2011, **133**, 7296.

23 W. Chen, C. Wang, K. Sasaki, N. Marinkovic, W. Xu, J. T. Muckerman, Y. Zhu, R. R. Adzic, *Energ. & Environ. Sci.*, 2013, **6**, 943.

24 Z. C. Xing, Q. Liu, A. M. Asiri, X. P. Sun, *Adv. Mater.*, 2014, **26**, 5702.

25 J. Kibsgaard, Z. B. Chen, B. N. Reinecke, T. F. Jaramillo, *Nat. Mater.*, 2012, **11**, 963.

26 D. Merki, S. Fierro, H. Vrubel, X. L. Hu, *Chem. Sci.*, 2011, **2**, 1262.

27 D. S. Kong, H. T. Wang, Z. Y. Lu, Y. Cui, $CoSe_2$, *J. Am. Chem. Soc.*, 2014, **136**, 4897.

28 W. F. Chen, K. Sasaki, C. Ma, A. I. Frenkel, N. Marinkovic, J. T. Muckerman, Y. M. Zhu, R. R. Adzic, *Angew. Chem. Int. Ed.*, 2012, **51**, 6131.

29 J. Yang, D. Voiry, S. J. Ahn, D. Kang, A. Y. Kim, M. Chhowalla, H. S. Shin, *Angew. Chem. Int. Ed.*, 2013, **52**, 13751.

30 Q. Li, , Z. C. Xing, A. M. Asiri, P. Jiang, X. P. Sun, *Int. J. Hydrogen Energ.*, 2014, **39**, 16806.

31 Z. H. Pu, Q. Liu, C. Tang, A. M. Asiribc, X. P. Sun, *Nanoscale*, 2014, **6**, 11031.

32 P. Jiang, Q. Liu, X. P. Sun, *Nanoscale*, 2014, **6**, 13440.

33 H. Tang, K. P. Dou, C. C. Kaun, Q. Kuang, S. H. Yang, *J. Mater. Chem. A*, 2014, **2**, 360.

34 W. Cui, Q. Liua, Z. C. Xing, A. M. Asiri, K. A. Alamry, X. P. Sun, *Appl. Catal. B*, 2015, **164**, 144.

35 J. Q. Tian, Q. Liu, N. Y. Cheng, A. M. Asiri, X. P. Sun, *Angew. Chem. Int. Ed.*, 2014, **53**, 9577.

36 P. Jiang, Q. Liu, Y. H. Liang, J. Q. Tian, A. M. Asiri, X. P. Sun, *Angew. Chem. Int. Ed.,* 2014, **53**, 1.

37 Y. Liang, Q. Liu, A. M. Asiri, X. Sun, Y. Luo, *ACS Catal.* 2014, **4**, 4065.

38 (a) A.B. Laursen, S. Kegnaes, S. Dahl, I. Chorkendorff, *Energy Environ. Sci.*, 2012, 5, 5577-5591. (b) Y. F. Xu, M. R. Gao, Y. R. Zheng, J. J. Jiang, S. H. Yu, *Angew. Chem. Int. Ed.*, 2013, **52**, 8546.

39 (a) J. Xie, H. Zhang, S. Li, R. Wang, X. Sun, M. Zhou, J. Zhou, X. Lou, Y. Xie, *Adv. Mater.*, 2013, **25**, 5807; (b) S. Gu, H. Du, A. M. Asiri, X. Sun, C. M. Li, *Phys. Chem. Chem. Phys.*, 2014, **16**, 16909.

40 H. Vrubel, T. Moehl, M. Gratzel, X. Hu, *Chem. Commun.*, 2013, **49**, 8985.

41 H. F. Du, Q. Liu, N. Y. Cheng, A. M. Asiri, X. P. Sun, C. M. Li, *J. Mater. Chem. A*, 2014, **2**, 14812.

42 Y. Nicolet, A. L. de Lacey, X. Vernede, V. M. Fernandez, E. C. Hatchikian, J. C. Fontecilla-Camps, *J. Am. Chem. Soc.*, 2001, **123**, 1596.

43 A. D. Wilson, R. K. Shoemaker, A. Miedaner, J. T. Muckerman, D. L. DuBois, M. R. DuBois, *Proc. Natl. Acad. Sci. U. S. A*, 2007, **104**, 6951.

44 P. Liu, J. A. Rodriguez, *J. Am. Chem. Soc.*, 2005, **127**, 14871.

45 W. Zhang, J. D. Hong, J. W. Zheng, Z. Y. Huang, J. R. Zhou, R. Xu, *J. Am. Chem. Soc.*, 2011, **133**, 20680.

Figure Captions

Scheme 1. Synthesis of Ni_2P/CNT nanohybrid by the in-situ thermal decomposition.

Fig. 1. XRD patterns for (a) CNT, (b) Ni/CNT, (c) $Ni_{12}P_5$/CNT and (d) Ni_2P/CNT.

Fig. 2. TEM and HRTEM images of (a, b) Ni/CNT, (c, d) $Ni_{12}P_5$/CNT and (e, f) Ni_2P/CNT.

Fig. 3. XPS spectra of (a) survey spectrum, (b) C 1s, (c) Ni 2p and (d) P 2p regions for Ni_2P/CNT.

Fig. 4. (a) LSV curves of the Ni_2P/CNT, $Ni_{12}P_5$/CNT, Ni/CNT, Pt/C, CNT and bare GCE in 0.5 M H_2SO_4 with a scan rate of 5 $mV \cdot s^{-1}$. (b) Tafel plots of the Ni_2P/CNT, $Ni_{12}P_5$/CNT, Ni/CNT and Pt/C. (c) Calculated TOFs for the Ni_2P/CNT, $Ni_{12}P_5$/CNT and Ni/CNT in 0.5 M H_2SO_4. (d) Time-dependent current density curve of the Ni_2P/CNT nanohybrid under static overpotential of 150 mV. Inserted is the Polarization curves of Ni_2P/CNT in 0.5 M H_2SO_4 initially and after 500 CV sweeps.

Fig. 5. (a) Nyquist plots and (b) Bode plots of the Ni_2P/CNT nanohybrid 0.5 M H_2SO_4. (c) Tafel slope fitted from EIS data measured in 0.5 M H_2SO_4. (d) Nyquist plots of Ni_2P/CNT, $Ni_{12}P_5$/CNT and Ni/CNT in 0.5 M H_2SO_4 with an overpotential of 200 mV. Inserted is an expansion of the high frequency region.

Fig. 6. Fig. 6. The amount of H_2 theoretically calculated (red line) and experimentally measured versus time for Ni_2P/CNT (black line) and $Ni_{12}P_5$/CNT (blue line) at 0.5 M H_2SO_4 under a static current density of 20 mA cm^{-2} for 30 min, respectively.

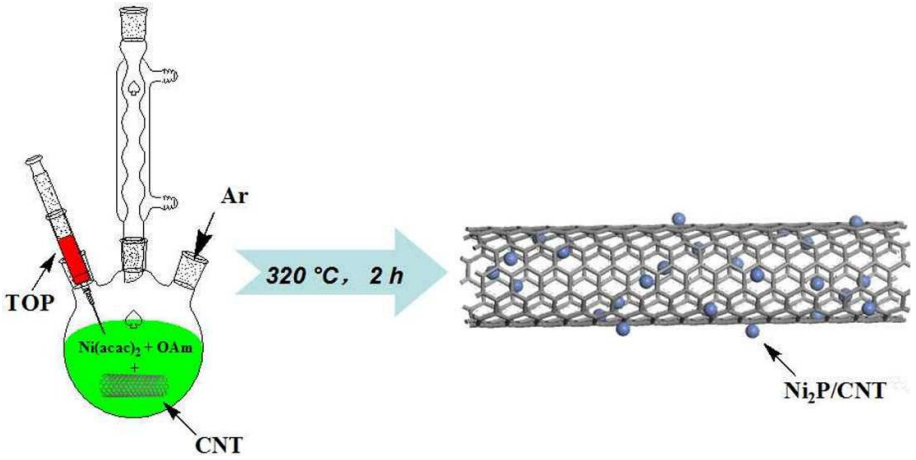

Scheme 1. Synthesis of Ni_2P/CNT nanohybrid by the in-situ thermal decomposition.

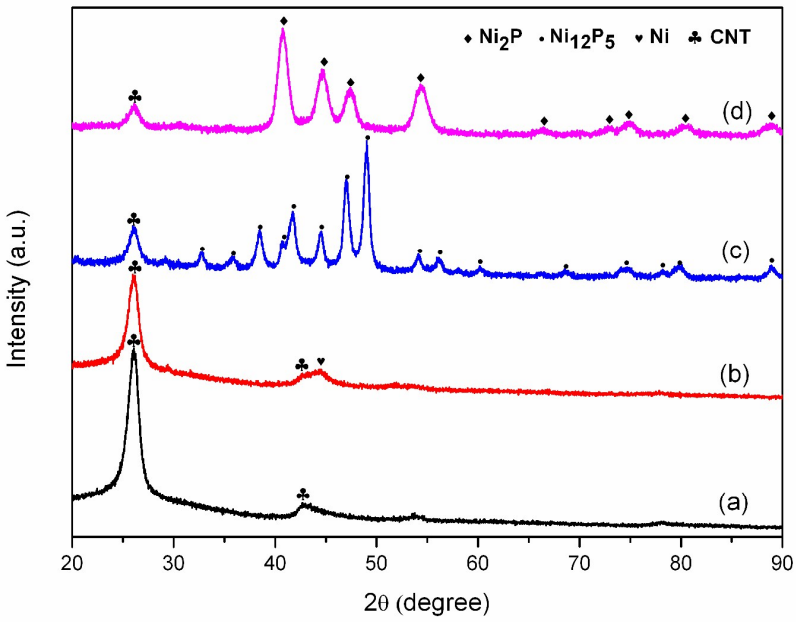

Fig. 1. XRD patterns for (a) CNT, (b) Ni/CNT, (c) $Ni_{12}P_5$/CNT and (d) Ni_2P/CNT.

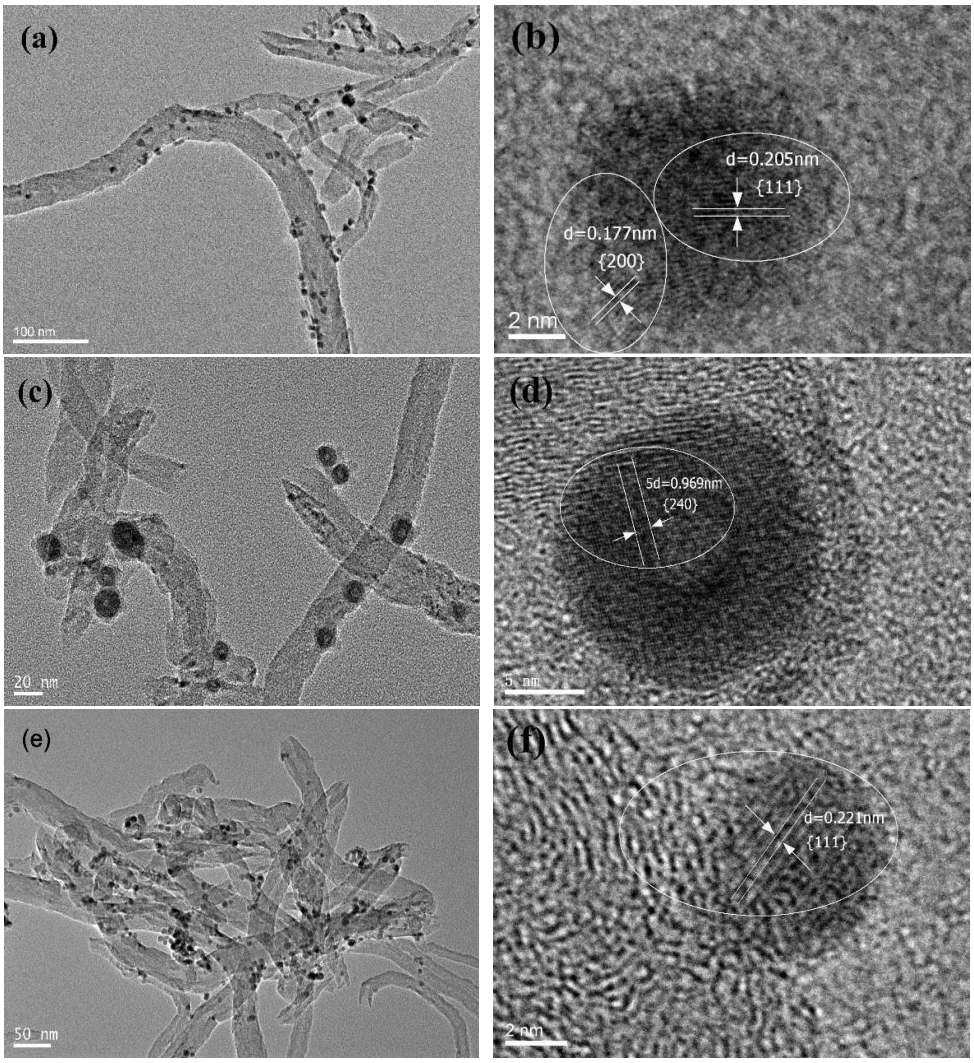

Fig. 2. TEM and HRTEM images of (a, b) Ni/CNT, (c, d) $Ni_{12}P_5$/CNT and (e, f) Ni_2P/CNT.

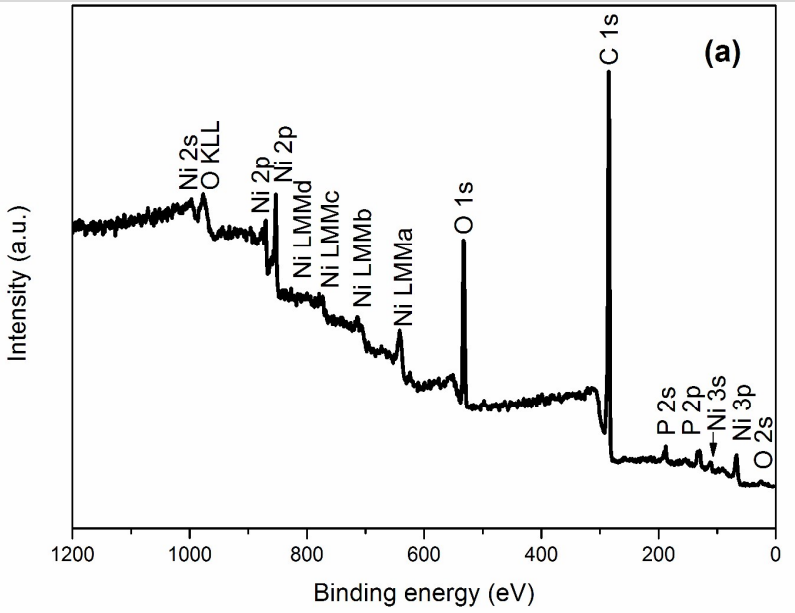

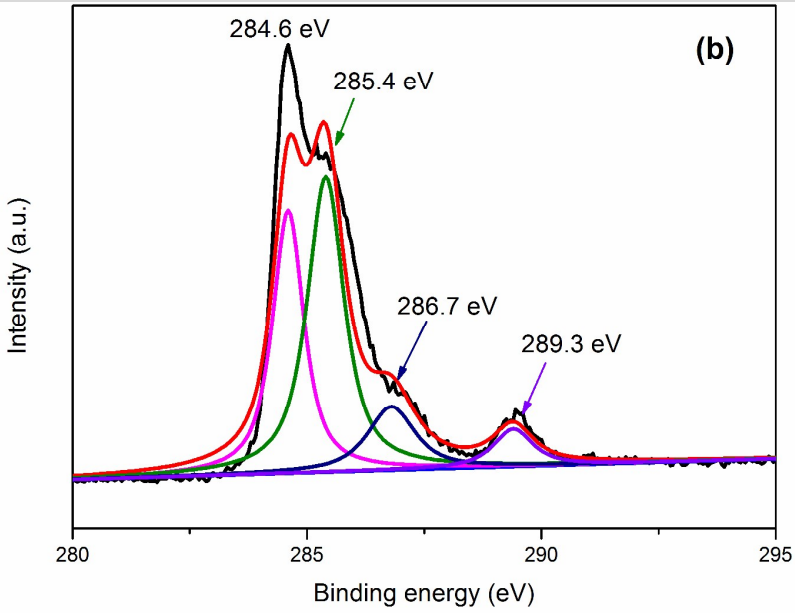

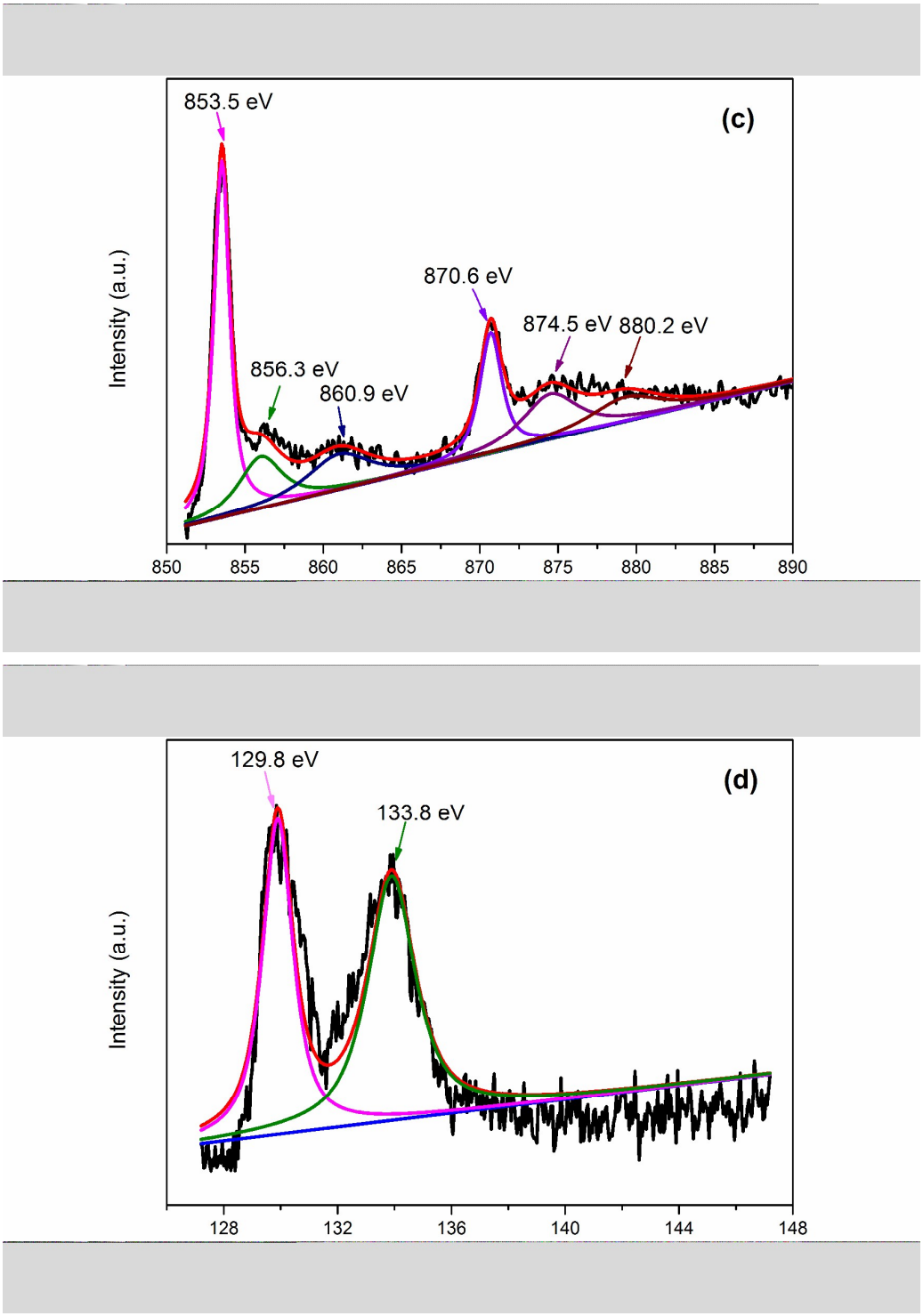

Fig. 3. XPS spectra of (a) survey spectrum, (b) C 1s, (c) Ni 2p and (d) P 2p regions for Ni_2P/CNT.

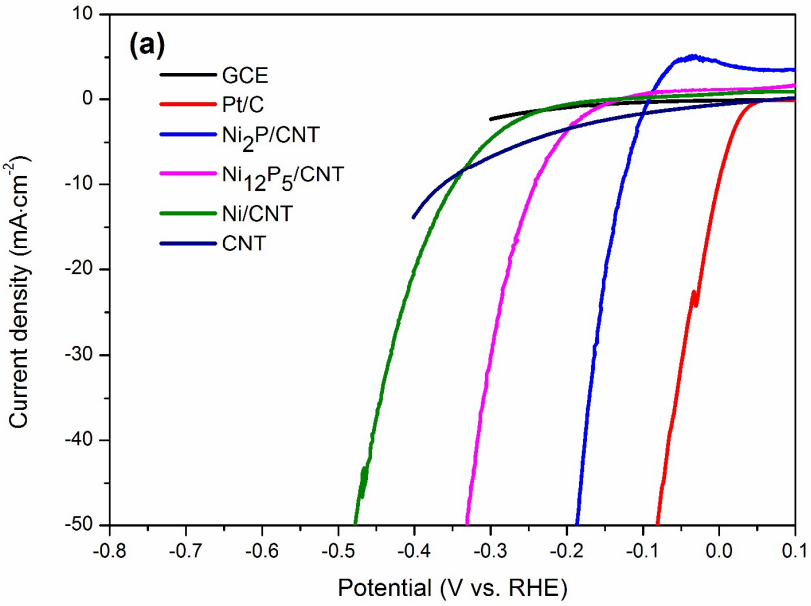

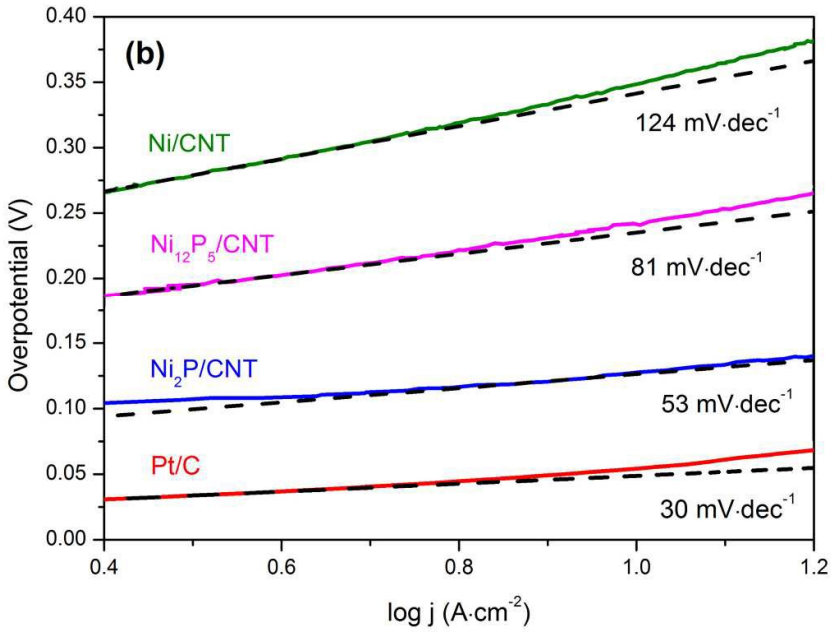

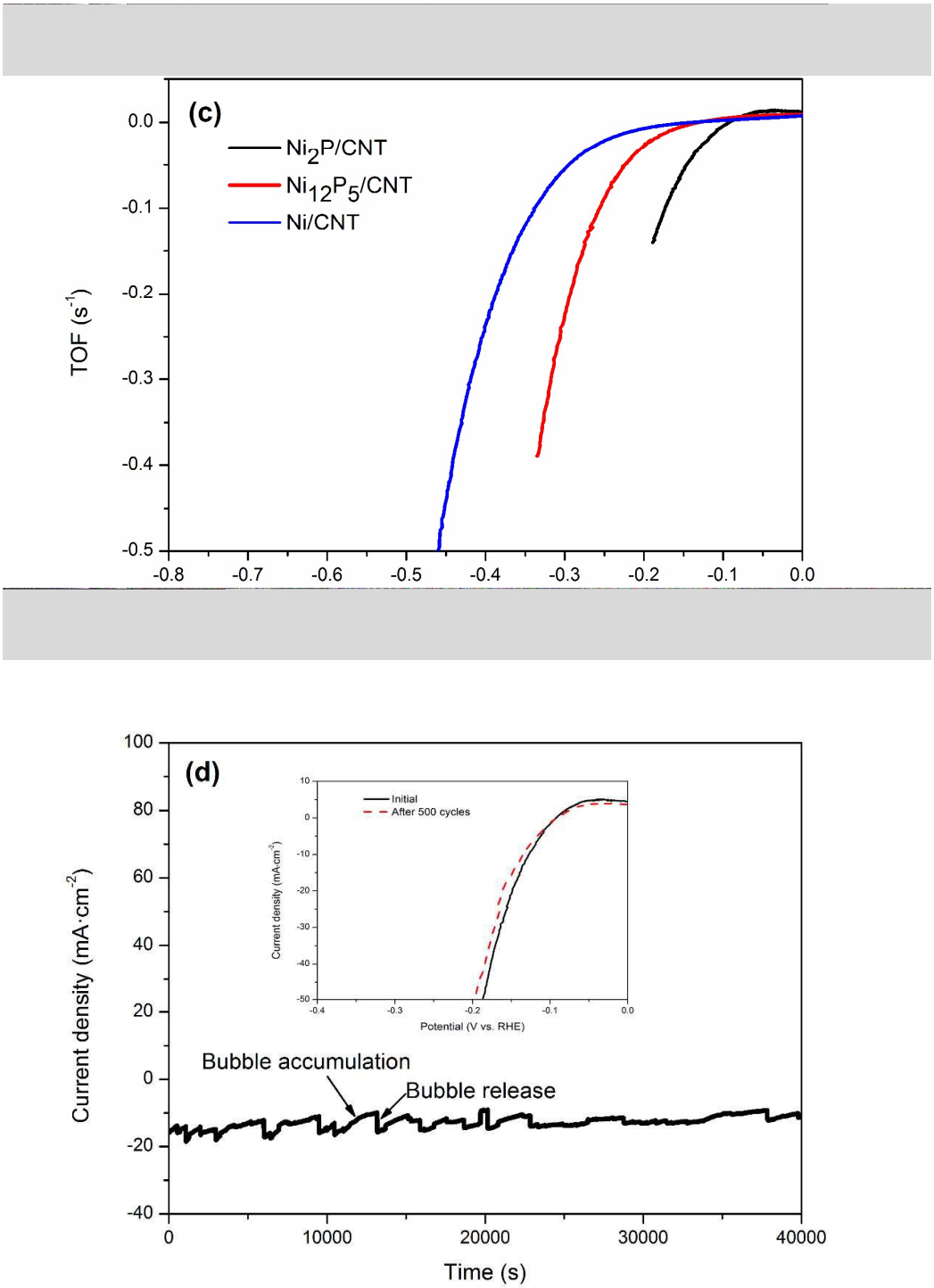

Fig. 4. (a) LSV curves of the Ni_2P/CNT, $Ni_{12}P_5$/CNT, Ni/CNT, Pt/C, CNT and bare GCE in 0.5 M H_2SO_4 with a scan rate of 5 $mV \cdot s^{-1}$. (b) Tafel plots of the Ni_2P/CNT, $Ni_{12}P_5$/CNT, Ni/CNT and Pt/C. (c) Calculated TOFs for the Ni_2P/CNT, $Ni_{12}P_5$/CNT

and Ni/CNT in 0.5 M H_2SO_4. (d) Time-dependent current density curve of the Ni_2P/CNT nanohybrid under static overpotential of 150 mV. Inserted is the Polarization curves of Ni_2P/CNT in 0.5 M H_2SO_4 initially and after 500 CV sweeps.

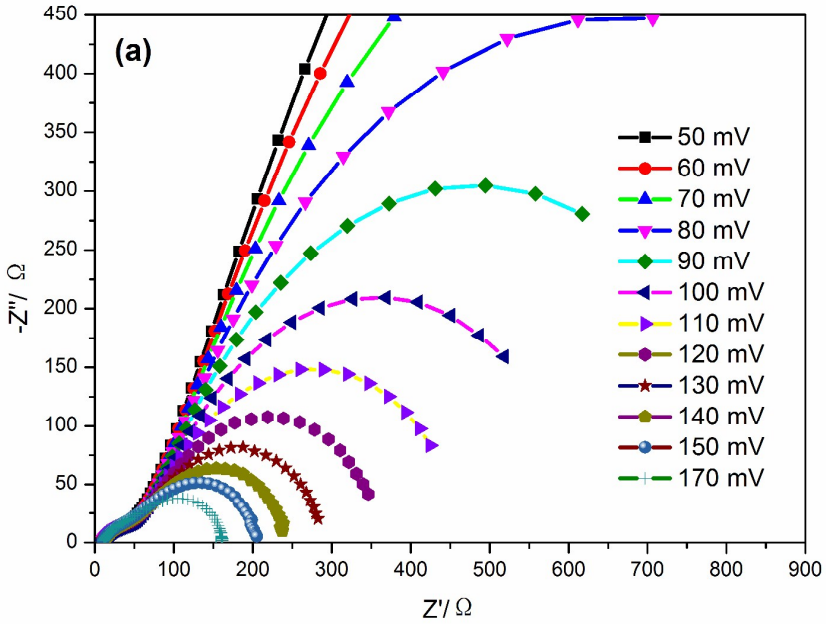

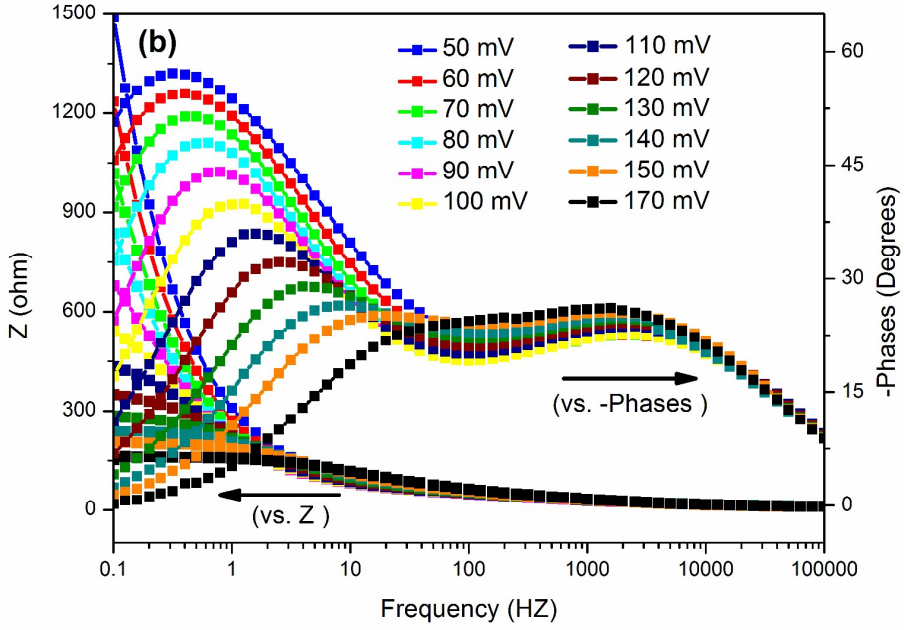

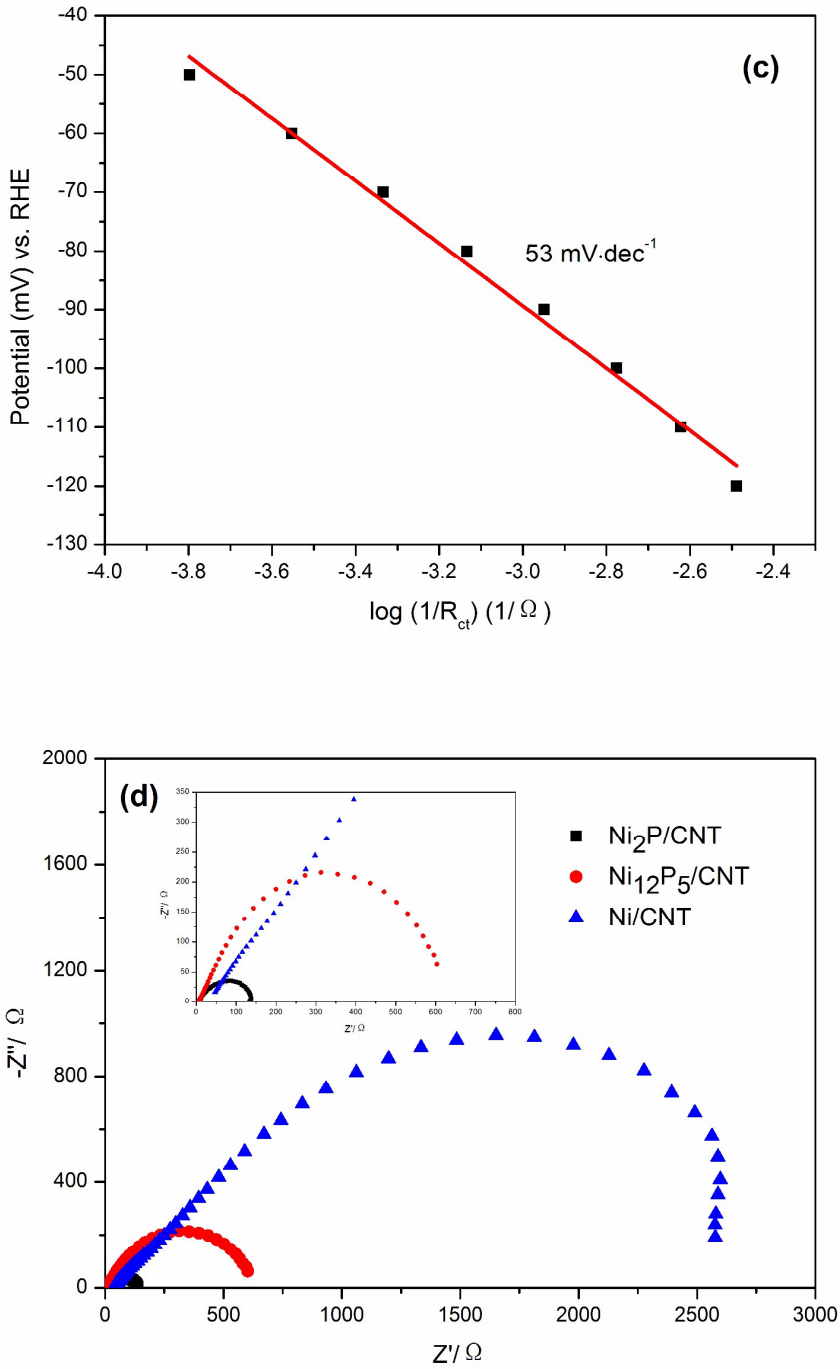

Fig. 5. (a) Nyquist plots and (b) Bode plots of the Ni_2P/CNT nanohybrid 0.5 M H_2SO_4. (c) Tafel slope fitted from EIS data measured in 0.5 M H_2SO_4. (d) Nyquist plots of Ni_2P/CNT, $Ni_{12}P_5$/CNT and Ni/CNT in 0.5 M H_2SO_4 with an overpotential of 200 mV.

Inserted is an expansion of the high frequency region.

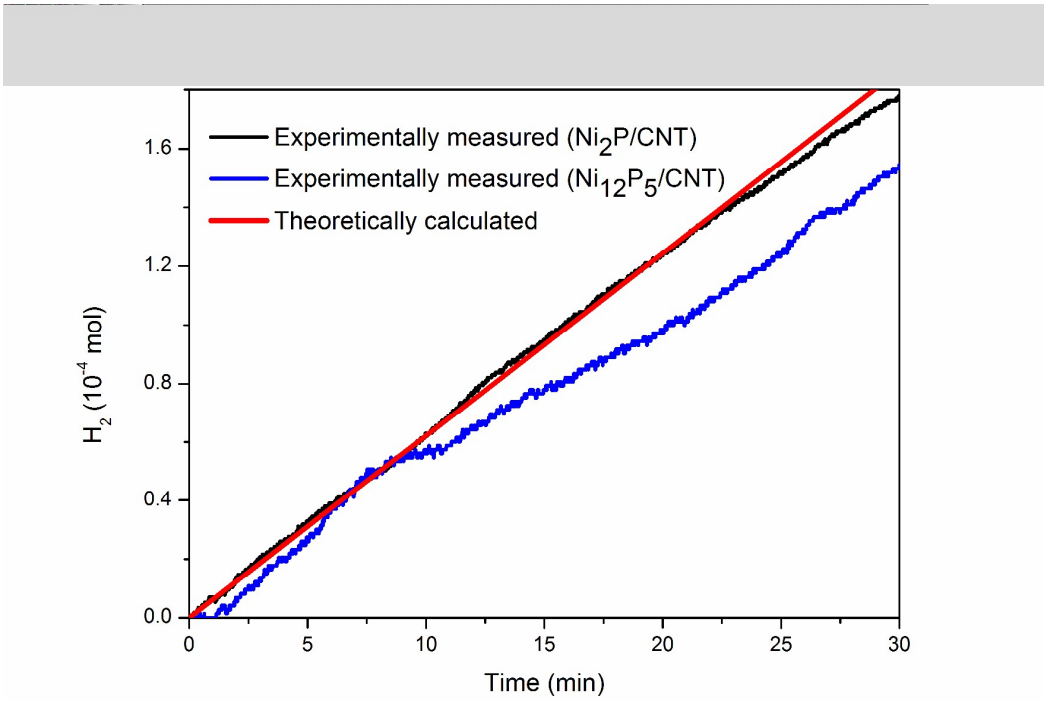

Fig. 6. The amount of H_2 theoretically calculated (red line) and experimentally measured versus time for Ni_2P/CNT (black line) and $Ni_{12}P_5$/CNT (blue line) at 0.5 M H_2SO_4 under a static current density of 20 mA cm^{-2} for 30 min, respectively.

Table 1 ICP-MS analysis results of the as-synthesized Ni_2P/CNT and $Ni_{12}P_5$/CNT nanohybrids.

Catalyst	Element content (Ni, ω %)	Element content (P, ω %)
Ni_2P/CNT	49.07	14.76
$Ni_{12}P_5$/CNT	67.68	17.42

Graphic Abstract

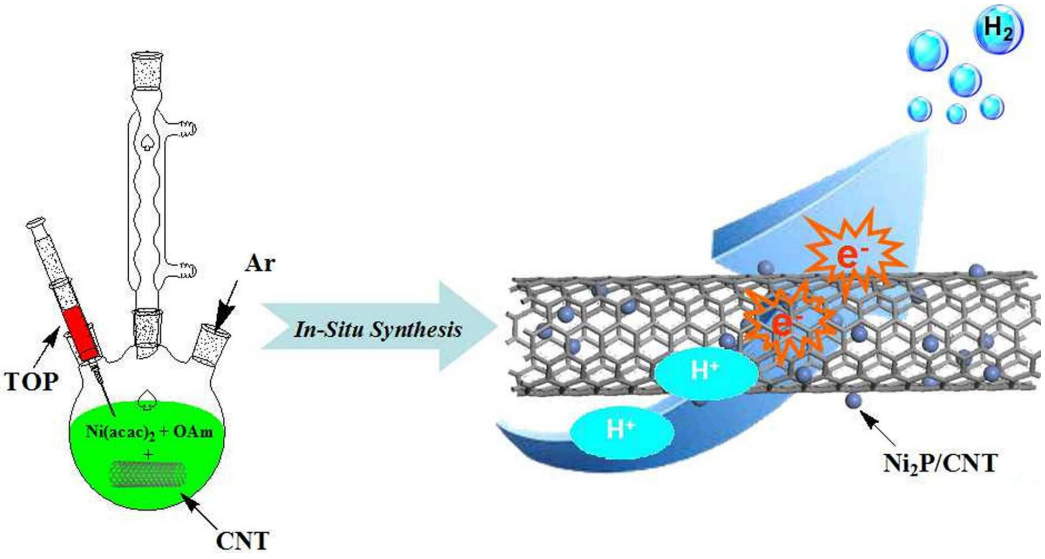

Nickel phosphide nanoparticles decorated on multiwall carbon nanotubes (Ni_2P/CNT) was synthesized by in situ thermal decomposition for the first time. The Ni_2P/CNT nanohybrid exhibits high activity and stability for the hydrogen evolution reaction.

.